

Rovibrational transitions in HCl due to collisions with H₂: spin-free and hyperfine-resolved transitions

DANIEL HOFFMAN,¹ JOSIAH TAYLOR,¹ T. J. PRICE^{1,2}, ROBERT C. FORREY¹, B. H. YANG³, P. C. STANCIL³,
Z. E. ZHANG,⁴ AND N. BALAKRISHNAN⁵

¹*Department of Physics, Penn State University, Berks Campus, Reading, PA 19610-6009, United States*

²*Department of Mathematics and Technology, Alvernia University, Reading, PA 19607-1737*

³*Department of Physics and Astronomy and the Center for Simulational Physics, University of Georgia, Athens 30602, United States*

⁴*RIKEN, Hirosawa 2-1, Wako, Saitama 351-0198, Japan*

⁵*Department of Chemistry and Biochemistry, University of Nevada, Las Vegas, NV 89154, United States*

(Received September 14, 2023; Revised; Accepted)

Submitted to ApJ

ABSTRACT

Hydrogen chloride (HCl) is a key repository of chlorine in the interstellar medium. Accurate determinations of its abundance is critical to assessing the chlorine elemental abundance and constraining stellar nucleosynthesis models. To aid in modeling recent and future observations of HCl rovibrational spectra, we present cross sections and rate coefficients for collisions between HCl and molecular hydrogen. Transitions between rovibrational states of HCl are considered for temperatures ranging from 10 to 3000 K. Cross sections are computed using a full dimensional quantum close-coupling (CC) method and a reduced dimensionality coupled-states (CS) approach. The CS results, benchmarked against the CC results, are used with a recoupling approach to calculate hyperfine-resolved rate coefficients for rovibrational transitions of HCl induced by H₂. The rate coefficients will allow for a better determination of the HCl abundance in the interstellar medium and an improved understanding of interstellar chlorine chemistry. We demonstrate the utility of the new rate coefficients in a non-thermodynamic equilibrium radiative transfer model applied to observations of HCl rovibrational transitions in a circumstellar shell.

Keywords: molecular processes

1. INTRODUCTION

Accurate rovibrational rate coefficients for molecular collisions involving H₂ are needed to interpret submillimeter and infrared observations of interstellar gas that is irradiated by strong UV sources, which often drives level populations out of local thermodynamic equilibrium (LTE). In such cases, which are typical of the ISM, photodissociation regions (PDRs), and upper layers of protoplanetary disks (PPDs), a non-LTE (NLTE) analysis is required in which the level populations are obtained by consideration of the relevant microphysical processes. However, NLTE studies of most molecular species is limited to rotational transitions due to the sparsity of collisional data for rovibrational transitions, particularly for H₂ impact.

HCl has been detected in the atmospheres of some planets (Olsen 2021; Korabev 2021; Krasnopolsky 2010; Teanby et al. 2021), as well as in interstellar clouds (Blake et al. 1985; Schilke et al. 1995; Cernicharo et al. 2010; Peng et al. 2010; Codella et al. 2011). It is an important tracer of chlorine and can be used to constrain the chlorine elemental abundance and isotope ratios (Monje et al. 2013; Lanza et al. 2014a). In 2013, for the first time, the fundamental vibration-rotation band of HCl (X ¹Σ⁺) was detected within the dense environment of a circumstellar shell (Goto et al. 2013). The observed levels in the $v = 0 \rightarrow 1$ fundamental band, observed in absorption, could be populated by collisions between para- or ortho-H₂ and HCl. Rate coefficients that include this mechanism would predominantly involve transitions from HCl ($v = 0, j = 1\text{--}20$), HCl ($v = 1, j = 1\text{--}10$), and HCl ($v = 2, j = 1\text{--}10$), where v and j

are the vibrational and rotational quantum numbers, respectively. Unfortunately, there have been no reported rate coefficients for rovibrational transitions in HCl due to collision with H₂.

Rate coefficients for rotational transitions in HCl ($v = 0$, $j = 1-5$) were computed by Lanza et al. (2014b) for temperatures from 5 to 300 K. These calculations used a rigid rotator approximation for both molecules in a four-dimensional close-coupling (4D-CC) formulation. Scattering calculations involving higher vibrational levels of HCl have been facilitated by the first full-dimensional (6D) potential energy surface (PES) for HCl-H₂, which was calculated by Yao et al. (2019). In that work, the 6D PES was reduced to a 4D PES, and the resulting 4D-CC calculations yielded rate coefficients that were within 10–20% of those reported by Lanza et al. (2014b). Subsequent 6D-CC calculations were performed using the 6D PES (Yao et al. 2019); pure rotational quenching from HCl ($v = 1$, $j = 2$) induced by para-H₂ was investigated for collision energies ranging from 10^{-4} to 1 cm^{-1} (Morita et al. 2020), as well as transitions from HCl ($v = 0$, $j = 0$) to HCl ($v' = 0$, $j' = 1$) induced by para-H₂ for collision energies from 100 to 6000 cm^{-1} (Morita et al. 2021). None of these studies, however, considered changes in vibrational quantum number.

In the present work, scattering calculations for HCl+H₂ are extended to higher rotational quantum numbers and collision energies, and full rovibrational inelasticity is considered. Cross sections and rate coefficients are reported for transitions from HCl ($v = 0$, $j = 1-20$) and HCl ($v = 1$, $j = 1-10$) induced by para- and ortho-H₂. For selected transitions, 6D-CC calculations are performed for temperatures from 10 to 1000 K. A reduced-dimensionality coupled-states approximation (referred to as 5D-CS) is used to determine cross sections and rate coefficients for higher rotational levels and temperatures (up to 3000 K) for which the 6D-CC calculations are computationally demanding.

Rate coefficients for hyperfine-resolved transitions of HCl are also reported. These rate coefficients were determined by using a recoupling approach with the 5D-CS spin-free T -matrices and are compared with those determined by Lanza & Lique (2014), who also used a recoupling approach with their spin-free calculations for rigid rotator HCl + H₂. The rate coefficients of Lanza & Lique (2014) have been used in astrophysical models incorporating observations from the Herschel Space Observatory and Caltech Submillimeter Observatory facilities (Kama 2015). Here, we perform a NLTE model for the HCl fundamental vibrational absorption band observed in the circumstellar shell of CR 2136 (Goto et al. 2013) and provide line ratio diagnostics.

This manuscript is divided into the following sections. The 6D potential energy surface is discussed in Section 2, and the theoretical methods used to perform the scattering calculations are discussed in Section 3. Section 4 presents cross sections and rate coefficients for rovibrational transitions of HCl, while Section 5 presents hyperfine-resolved results. In Section 6, the current rate coefficients are used to model interstellar environments in NLTE, while conclusions are presented in Section 7.

2. POTENTIAL ENERGY SURFACE

The scattering calculations reported in the present work used a 6D PES for the HCl+H₂ system (Yao et al. 2019). This PES was computed and trained with machine learning; the machine learning algorithm utilized a training set of 42,417 *ab initio* points, which were determined by using the coupled-cluster method with singles, doubles, and perturbative triples excitations.

The PES is specified in terms of the Jacobi coordinates (R , r_1 , r_2 , θ_1 , θ_2 , ϕ) shown in Fig. 1, where r_1 and r_2 denote the HCl and H₂ internuclear separations, R is the separation between the center-of-mass of the two molecules, θ_1 and θ_2 are the two Jacobi angles, and ϕ denotes the dihedral, or relative twist, angle between the two molecules. The potential exhibits two T-shaped minima as shown in Fig. 2. A global minimum of 216 cm^{-1} arises when H₂ is on

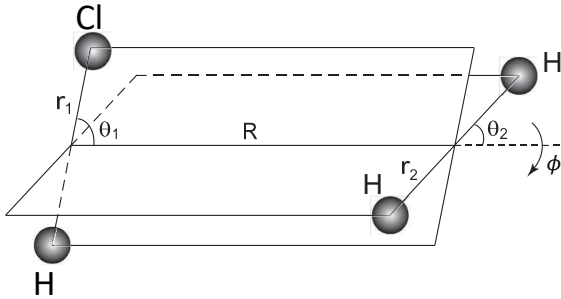


Figure 1. Jacobi coordinate system for HCl+H₂.

the H side of HCl. The secondary minimum of 96 cm^{-1} arises when H_2 is on the Cl side. The configurations associated with these minima are consistent with an experimental study by [Anderson et al. \(1998\)](#) and with theoretical work by [Alkorta et al. \(2010\)](#) and [Lanza et al. \(2014b\)](#). The well depths of the 6D potential are slightly different than in the 4D PES computed by [Lanza et al. \(2014b\)](#); the global and secondary minima in the 4D potential were 213 and 99 cm^{-1} , respectively.

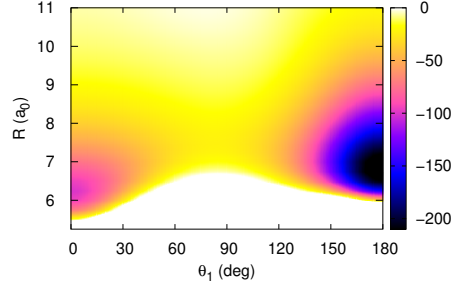
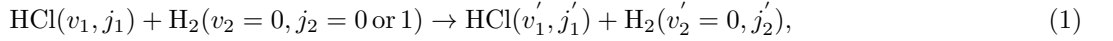


Figure 2. Color map of the 6D PES [Yao et al. \(2019\)](#) in cm^{-1} as a function of R and θ_1 with fixed $r_1 = 2.55 a_0$, $r_2 = 1.40 a_0$, $\theta_2 = 90^\circ$, and $\phi = 0^\circ$. The two T-shaped minima are shown as potential wells.

3. THEORETICAL METHODS

Two different sets of scattering calculations (6D-CC and 5D-CS) were performed for the following collision processes:



where v_1 and j_1 are the vibrational and rotational quantum numbers of HCl, and v_2 and j_2 are the vibrational and rotational quantum numbers of H_2 . The quantum mechanical descriptions for the CC and CS scattering formulations have been given previously ([Alexander & DePristo 1977](#); [Green 1975](#); [Heil et al. 1978](#); [Forrey et al. 2015](#); [Yang et al. 2018](#); [Burton et al. 2018](#); [Yang et al. 2020](#); [Price et al. 2021](#)). Here a brief summary is included.

The scattering calculations involve expanding the wave function for the system in a basis set of products of molecular wave functions $\chi_{v_1, j_1}(r_1)\chi_{v_2, j_2}(r_2)$ with vibrational and rotational quantum numbers v_i and j_i . A system of coupled equations of the form

$$\left[-\frac{\hbar^2}{2\mu} \frac{d^2}{dR^2} + \frac{\hbar^2 l(l+1)}{2\mu R^2} - E_c \right] F_n(R) + \sum_{n'} V_{n; n'}(R) F_{n'}(R) = 0, \quad (2)$$

is solved, with $E_c = E - E_n$. For the 6D-CC formulation, the channel index n is defined by the set of quantum numbers $\{v_1, v_2, j_1, j_2, j_{12}, l\}$, where l is the orbital angular momentum quantum number and $\vec{j}_{12} = \vec{j}_1 + \vec{j}_2$. The potential V -matrix and the transition T -matrix are diagonal with respect to the total angular momentum quantum number J defined by $\vec{J} = \vec{l} + \vec{j}_{12}$. The cross section is given by

$$\sigma_{n \rightarrow n'}^{6\text{D-CC}} = \frac{\pi}{k_n^2} [(2j_1 + 1)(2j_2 + 1)]^{-1} \sum_{j_{12} j'_{12} l l' J} (2J + 1) |T_{n; n'}^J|^2. \quad (3)$$

The 6D-CC calculations are fully exact up to limitations in the PES and in the truncation of the basis set. These calculations become computationally demanding for $v_1 > 1$ and for high j_1 , due to the large number of channels. For this reason, we perform and benchmark 5D-CS calculations. For these calculations, two approximations are invoked. The first is the usual CS approximation, which maintains the full dimensionality of the problem but replaces the orbital angular momentum quantum number l in the channel index with a constant average value \bar{l} . The cross section for this approximation is given by

$$\sigma_{n \rightarrow n'}^{6\text{D-CS}} = \frac{\pi}{k_n^2} [(2j_1 + 1)(2j_2 + 1)]^{-1} \sum_{j_{12} j'_{12} \bar{l} \Omega} (2\bar{l} + 1) |T_{n; n'}^{\bar{l} \Omega}|^2, \quad (4)$$

where Ω is the quantum number for the projection of \vec{J} on the body-fixed z -axis, which is taken to lie along the direction of \vec{R} . The V -matrix is diagonal with respect to Ω , and the neglect of off-diagonal Coriolis coupling yields a

reduced T -matrix that is more efficient to compute. Nevertheless, the improvement in computational efficiency for the 6D-CS is modest due to the quantum number j_{12} , and it does not solve the bottleneck for states with high angular momentum. Therefore, we make the additional approximation

$$T_{n;n'}^{\bar{l}\Omega} = \sum_{m_1 m_2} \langle j_{12}\Omega | m_1 m_2 \rangle T_{n;n'}^{\bar{l}m_1 m_2} \langle m_1 m_2 | j'_{12}\Omega \rangle, \quad (5)$$

which assumes the \vec{j}_1 and \vec{j}_2 projection quantum numbers m_1 and m_2 do not change during the collision. This is equivalent to assuming the scattering is insensitive to the relative twist angle, ϕ . As a result of this approximation, the PES may be reduced from 6D to 5D, and j_{12} may be removed from the channel index n . The set of coupled equations in Eq. 2 is now substantially reduced in size without freezing out the vibrational flexibility. Substituting (5) into (4) yields the desired cross section

$$\sigma_{n \rightarrow n'}^{5D-CS} = \frac{\pi}{k_n^2} [(2j_1 + 1)(2j_2 + 1)]^{-1} \sum_{\bar{l}m_1 m_2} (2\bar{l} + 1) \left| T_{n;n'}^{\bar{l}m_1 m_2} \right|^2. \quad (6)$$

Figure 3 shows a representative plot of the dependence of the HCl+H₂ PES on ϕ ; the most significant dependence arises near the potential well. Previous studies (Forrey et al. 2015; Price et al. 2021) for CO-H₂ and SO-H₂ showed that a similar level of sensitivity to ϕ occurs closer to the repulsive wall and does not lead to substantial differences between 5D-CS and 6D-CS results. In the present system, averaging over ϕ may introduce some significant differences between the two CS approximations for vibrationally inelastic transitions that occur in the vicinity of the potential well.

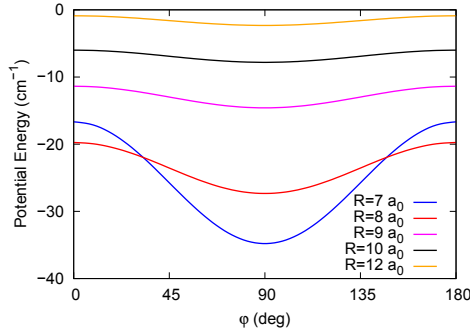


Figure 3. Potential energy as a function of twist angle ϕ for fixed intermolecular separations R , with $\theta_1 = \theta_2 = 90^\circ$, and each molecule near its equilibrium separation. The greatest dependence on twist angle occurs near the potential well.

Hyperfine-resolved transitions of HCl induced by H₂ were determined by using a recoupling approach (Lanza & Lique 2014; Corey & McCourt 1983; Offer et al. 1994) with the spin-free 5D-CS T -matrices. A similar approach with the 5D-CS approximation was shown to give reliable results for fine-structure transitions of CN (Burton et al. 2018) and SO (Price et al. 2021) induced by H₂. For HCl, the hyperfine structure arises primarily from coupling between the nuclear spin of the chlorine atom ($I = 3/2$) and the rotation of the molecule. To account for this coupling, the combined molecular state for HCl+H₂ needs to be generalized to $n = (\nu_1, j_1, F_1, \nu_2, j_2)$, where $\vec{F}_1 = \vec{j}_1 + \vec{I}_1$ and \vec{I}_1 is the nuclear spin of Cl. If the hyperfine energy splittings are small, the dynamics may be simplified using a degenerate approximation which allows the hyperfine transitions to be obtained from a recoupling of the spin-free T -matrix. Within the 5D-CS approximation, the hyperfine-resolved cross sections are given by

$$\sigma_{n \rightarrow n'}^{5D-CS} = \frac{\pi}{k_n^2} [(2F_1 + 1)(2j_2 + 1)]^{-1} \sum_{\bar{l}m_1 m_2 \mu_1} (2\bar{l} + 1) T_{n;n'}^{\bar{l}m_1 m_2} T_{n;n'}^{*\bar{l}m'_1 m'_2} \begin{pmatrix} I_1 & j_1 & F_1 \\ -m'_1 - \mu_1 & m'_1 & \mu_1 \end{pmatrix} \begin{pmatrix} I_1 & j_1 & F_1 \\ -m_1 - \mu_1 & m_1 & \mu_1 \end{pmatrix} \begin{pmatrix} I_1 & j'_1 & F'_1 \\ -m'_1 - \mu_1 & m'_1 & \mu_1 \end{pmatrix} \begin{pmatrix} I_1 & j'_1 & F'_1 \\ -m_1 - \mu_1 & m_1 & \mu_1 \end{pmatrix}, \quad (7)$$

where m_1 and μ_1 are the projection quantum numbers of j_1 and F_1 , respectively, \bar{l} is the effective orbital angular momentum quantum number, and (\cdots) is a Wigner $3j$ symbol.

Similar parameters were used for both the 6D-CC and 5D-CS scattering calculations. The radial coordinates of both molecules were represented as discrete variables with 10 points each, Gauss-Legendre quadratures were used for θ_1 and θ_2 with 14 points each, and a Chebyshev quadrature with 8 points was used for ϕ . The log-derivative matrix propagation method was used to integrate the set of coupled equations in Eq. 2. For the 6D-CC calculations, the grid ranged from $R = 0.95$ to $95 a_0$ in steps of $0.095 a_0$. For the 5D-CS calculations, results were computed at higher energies, and convergence was achieved with a grid ranging from $R = 1$ to $30 a_0$ in steps of $0.05 a_0$. For $v_1 = 1$, the 6D-CC calculations involved an HCl basis with $j_1 = 0$ to 25 for $v_1 = 0$ and $j_1 = 0$ to 15 for $v_1 = 1$. The 5D-CS basis set included $j_1 = 0$ to 40 for $v_1 = 0$ and $j_1 = 0$ to 30 for $v_1 = 1$; this enlarged basis set was needed for vibrationally inelastic transitions from $v_1 = 1$ when the collision energy was above 4000 cm^{-1} . The basis set for H_2 allowed for rotational excitation to the first excited rotational level ($j_2 = 2$ or 3), except for higher rotational levels ($v_1 = 0, j_1 > 10$) where it was important to include ($j_2 = 4$ or 5); this is discussed in the next section.

4. ROVIBRATIONAL TRANSITIONS OF HCL

4.1. Rotationally inelastic, vibrationally elastic transitions

Figure 4 compares 6D-CC and 5D-CS cross sections for rotationally inelastic transitions from $\text{HCl}(v_1 = 0, j_1 = 0)$ induced by para- H_2 . The 6D-CC and 5D-CS results show the same qualitative behavior, with percent differences generally within 20%. At lower collision energies, the cross sections follow the energy gap rule, decreasing with an increase in the energy gap. As the collision energy increases, the ordering of the curves changes; a propensity for $\Delta j = 2$ transitions develops, and the cross section for $\Delta j = 5$ increases significantly, becoming larger than $\Delta j = 3$ and 4.

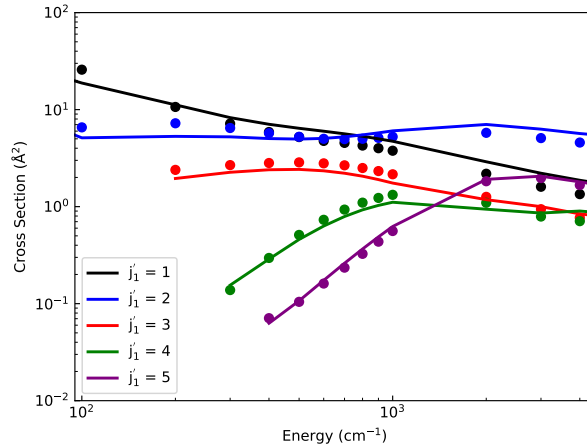


Figure 4. Comparison between rotational excitation cross sections for $\text{HCl}(v_1 = 0, j_1 = 0)$ induced by para- $\text{H}_2(v_2 = 0, j_2 = 0)$ for different j_1' , with $j_2' = 0$. The 6D-CC results are shown as points, while the 5D-CS results are shown as lines.

Figure 5 shows a comparison of 5D-CS de-excitation rate coefficients induced by para- and ortho- H_2 with 4D-CC rigid rotator results computed by Lanza et al. (2014b). The 5D-CS and 4D-CC rate coefficients generally agree to within 30% for both para- and ortho- H_2 perturbors, except for the transitions $\text{HCl}(j_1 = 4 \text{ or } 5 \rightarrow 3)$ induced by ortho- H_2 , which are within 60%. As noted above, the 5D-CS and 6D-CC results agree to within 20%, so the discrepancies shown in Fig. 5 are largely due to differences in the PES that were used in the calculations. Both sets of calculations indicate that the transition rates tend to be larger when induced by ortho- H_2 . As noted by Lanza et al. (2014b), the collisions exhibit a propensity for $\Delta j_1 = \text{odd}$ transitions. This propensity, which is related to the anisotropy of the PES, vanishes with increasing $|\Delta j_1|$ due to the increasing internal energy and angular momentum gaps associated with the transitions.

It was found that using an enlarged basis for H_2 was important for $j_1 > 10$. For $j_1 \leq 10$, it is sufficient to include rotational states of H_2 up to $j_2 = 2$ or 3 . However, as j_1 increases, it becomes important to include the next higher

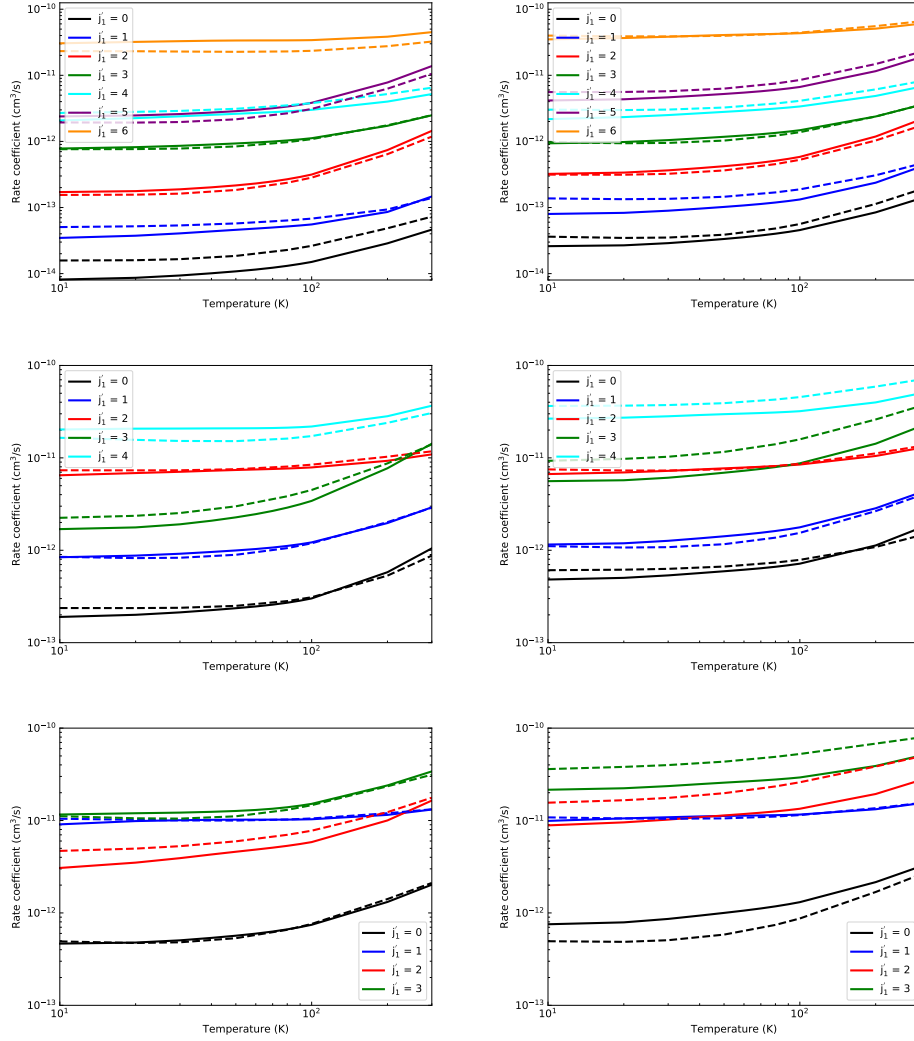


Figure 5. Comparison between 5D-CS rate coefficients (solid lines) and 4D-CC rigid rotator rate coefficients computed by [Lanza et al. \(2014b\)](#) (dashed lines). The curves show rotational de-excitation transitions $j_1 \rightarrow j_1'$ for HCl. Results for $j_1 = 7$ (top panels), $j_1 = 5$ (middle panels), and $j_1 = 4$ (bottom panels) are shown for transitions induced by para-H₂ (left panels) and ortho-H₂ (right panels). Note that for $j_1 = 7$, the rates are plotted on a different scale than for $j_1 = 4$ and 5.

rotational state of H₂. This is illustrated in Fig. 6, which shows cross sections for HCl($v_1 = 0$, $j_1 = 5, 10$, or 16)+para-H₂ obtained by including basis states up to $j_2 = 2$ or 4 . For $j_1 = 5$, the results are converged and it is not necessary to include a basis state for $j_2 = 4$. However, as j_1 increases, the results become less converged, particularly for larger Δj_1 . This is most clearly seen for $j_1 = 16$.

Figure 7 compares vibrationally elastic, rotationally inelastic 6D-CC and 5D-CS cross sections and rate coefficients for transitions HCl($v_1 = 1$, $j_1 = 5$)+H₂ \rightarrow HCl($v_1' = 1$, $j_1' = 0-4$)+H₂. Both the 6D-CC and 5D-CS cross sections and rate coefficients are larger for ortho-H₂ than para-H₂, as was the case for transitions within $v_1 = 0$. The cross sections for para-H₂ show a similar level of agreement as for rotationally inelastic transitions within $v_1 = 0$ (see Fig. 4). For para-H₂, both 6D-CC and 5D-CS show the same qualitative behavior, with the cross sections showing a propensity for $\Delta j_1 = \text{odd}$ transitions at lower energies, following the energy gap rule at intermediate energies, and showing a slight propensity for $\Delta j_1 = \text{even}$ transitions at higher energies. The agreement between 6D-CC and 5D-CS is, for the most part, similar for transitions induced by para- and ortho-H₂, with results generally differing by less than 30%; the exception is for HCl($v_1 = 1$, $j_1 = 5 \rightarrow 1, 3$)+ortho-H₂, where there is more of a discrepancy (between 30 and 60%), which results in a different ordering of the curves at low energies or temperatures.

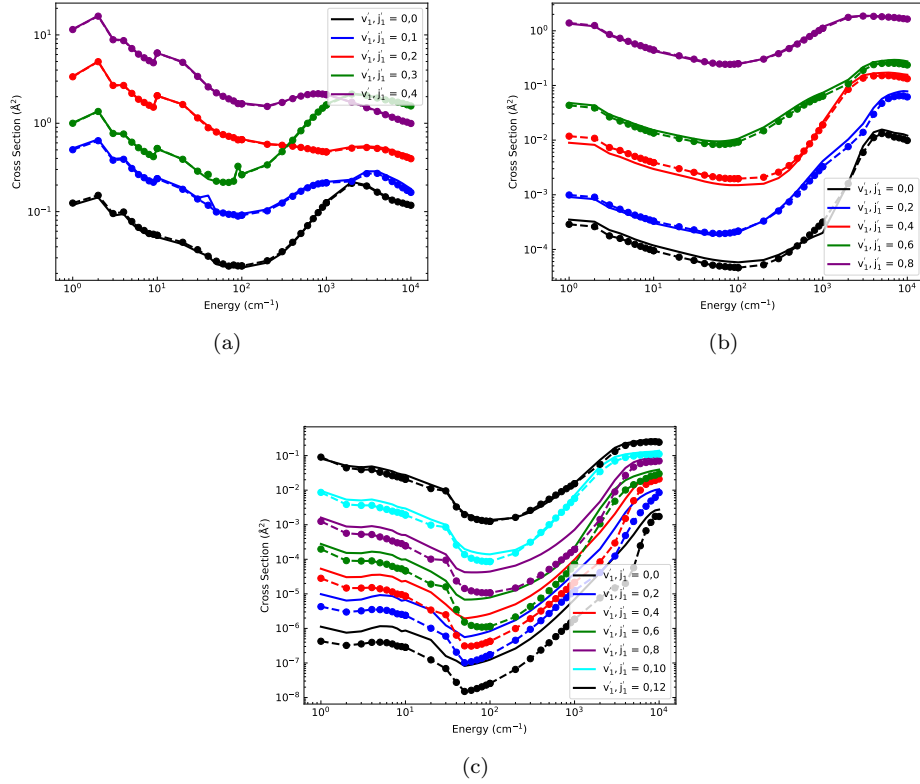


Figure 6. Comparison between 5D-CS cross sections for HCl+para-H₂ obtained by including basis states up to $j_2 = 2$ (solid lines), and $j_2 = 4$ (dashed lines with points). Results are shown for (a) $j_1 = 5$, (b) $j_1 = 10$, and (c) $j_1 = 16$.

4.2. *Vibrationally inelastic transitions*

Figure 8 shows 6D-CC cross sections for vibrational relaxation of HCl($v_1 = 1, j_1 = 0, 5$) induced by para- and ortho-H₂. The cross sections exhibit resonances due to the formation of quasi-bound states of HCl+H₂. These resonances are present for collision energies less than the well depth of the global minimum of the PES (below about 200 cm⁻¹). The prominent resonance near $E = 0.01$ cm⁻¹ for para-H₂ in panel (a) is due to an orbiting resonance in the $J = 3$ partial wave. This resonance disappears in the ortho-H₂ results shown in panel (b). A comparison between cross sections for $j_1 = 0$ and 5 shows that the resonances are less prevalent as j_1 increases.

Figure 9 compares 6D-CC and 5D-CS vibrational de-excitation cross-sections for the same transitions as in Fig. 8. The curves show similar qualitative behavior, but the relative errors in the 5D-CS results are larger for these transitions compared to pure rotational transitions due to the much smaller values for the cross sections. The 5D-CS results also do not resolve the resonances. This is because the positions of the resonances cannot be accurately determined within the CS approximation, and so the 5D-CS results were calculated on a coarser energy grid. Quantitatively, the 5D-CS results are consistently lower by at most a factor of two for $j_1 = 0$, by a factor of 5 for $j_1 = 5$ with para-H₂ as the perturber, and by a factor of 10 for $j_1 = 5$ with ortho-H₂ as the perturber.

Figure 10 compares 6D-CC and 5D-CS vibrational de-excitation rate coefficients for the same transitions as in Fig. 9. As expected, the rate coefficients show similar qualitative behavior, except for transitions from HCl($v_1 = 1, j_1 = 0$) induced by para-H₂ (Panel (a)). This is because of the large number of resonances; the agreement improves for transitions from HCl($v_1 = 1, j_1 = 5$) (Panel (c)). The smoother behavior of the rate coefficients may allow a superior machine learning approach to be developed for correcting the approximate rates than was previously developed for correcting the cross sections (Jasinski et al. 2020).

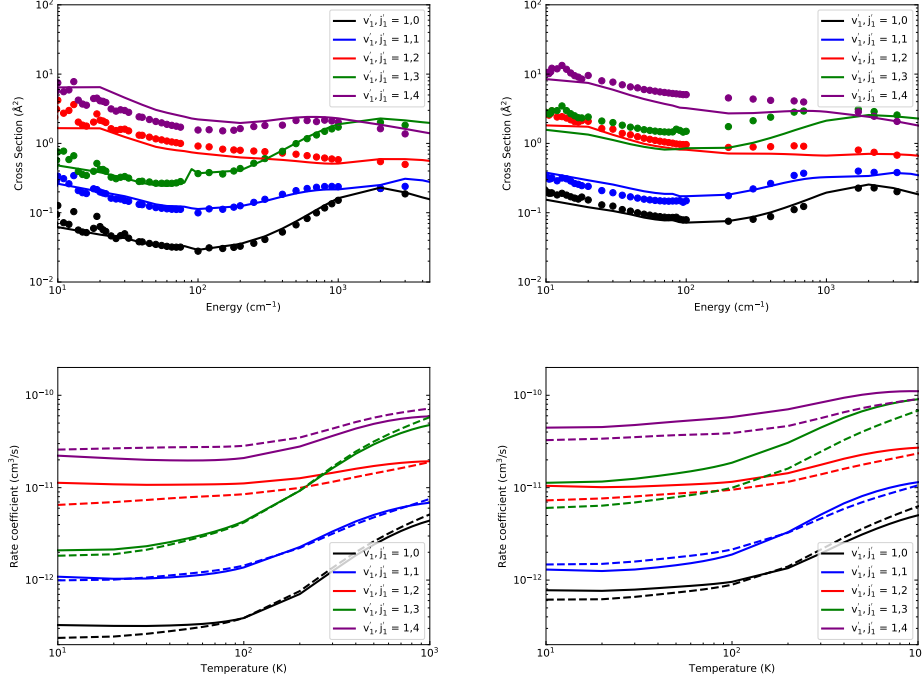


Figure 7. Comparison between 6D-CC and 5D-CS cross sections and rate coefficients for vibrationally elastic, rotationally inelastic transitions from $\text{HCl}(v_1 = 1, J_1 = 5)$ to $\text{HCl}(v'_1 = 1, j'_1 = 0 - 4)$ induced by collisions with H_2 . The upper panels compare cross sections as a function of collision energy, with 6D-CC results shown as points. The lower panels compare rate coefficients as a function of temperature, with 6D-CC results shown as solid lines. In the left panels, para- $\text{H}_2(v_2 = 0, j_2 = 0)$ is the perturber, while in the right panels ortho- $\text{H}_2(v_2 = 0, j_2 = 1)$ is the perturber.

5. HYPERFINE-RESOLVED TRANSITIONS

5.1. Rotationally inelastic, vibrationally elastic transitions

Hyperfine-resolved cross sections and rate coefficients were determined by using a recoupling approach and the 5D-CS spin-free T -matrices. For transitions within $v_1 = 0$, rate coefficients are compared with those determined by Lanza & Lique (2014), which are available from the BASECOL database (Dubernet et al. 2013).

Figure 11 compares selected 5D-CS and 4D-CC (Lanza & Lique 2014) rate coefficients for hyperfine transitions of $\text{HCl}(v_1 = 0, j_1 = 3, F_1 = 4.5)$ induced by H_2 . The curves show qualitative agreement, exhibiting the same ordering, with a propensity for $\Delta j_1 = \Delta F_1$ transitions, as expected. Both sets of curves show higher rates for transitions induced by ortho- H_2 , as was the case for the spin-free results. The present results for para- and ortho- H_2 collisions tend to be more similar than those given in the BASECOL database (e.g., see panels (c) and (d) where the BASECOL results are very different for the $\Delta j_1 \neq \Delta F_1$ transitions). This is generally the case for other transitions as well; for example, similar trends are exhibited in Fig. 12 for hyperfine transitions of $\text{HCl}(v_1 = 0, j_1 = 5, F_1 = 6.5)$ induced by H_2 .

We found that some of the BASECOL results appear to have unphysical behavior at higher temperatures. An example is shown in Fig. 12 for transitions of $\text{HCl}(v_1 = 0, j_1 = 5, F_1 = 6.5)$. At low temperatures, the curves are smooth and in reasonable agreement with the present results, however, the BASECOL results show sudden jumps at higher temperatures. This unphysical behavior was not seen in the spin-free results shown in Fig. 5. We noticed similar potentially unphysical behavior in the BASECOL database for the following transitions: (para- H_2): all transitions for $j = 5 \rightarrow 4$ and $j = 4 \rightarrow 0$; from $j = 4 \rightarrow 3$ for $F \rightarrow F' = 1.5$ and $4.5 \rightarrow 4.5$; $j = 5 \rightarrow 3$ for $5.5 \rightarrow 1.5$; $j = 5 \rightarrow 0$ for $6.5, 5.5$, and $4.5 \rightarrow 1.5$. (ortho- H_2): all transitions for $j = 5 \rightarrow 4$ except $5.5 \rightarrow 5.5$; all transitions from $j = 5$ and $4 \rightarrow 0$; from $j = 4 \rightarrow 3$ for $F \rightarrow 1.5$; from $j = 5 \rightarrow 3$ for $F \rightarrow F' = 4.5$ and 1.5 .

Figure 13 shows a comparison between hyperfine-resolved 5D-CS rate coefficients for vibrationally elastic, rotationally inelastic transitions within $v_1 = 0$ and $v_1 = 1$. The rate coefficients are very similar, as expected, and are often but not always a bit higher for $v_1 = 1$ than $v_1 = 0$. These rate coefficients should be reliable based on the good agreement with the spin-free 6D-CC results for vibrationally elastic transitions (see Fig. 7).

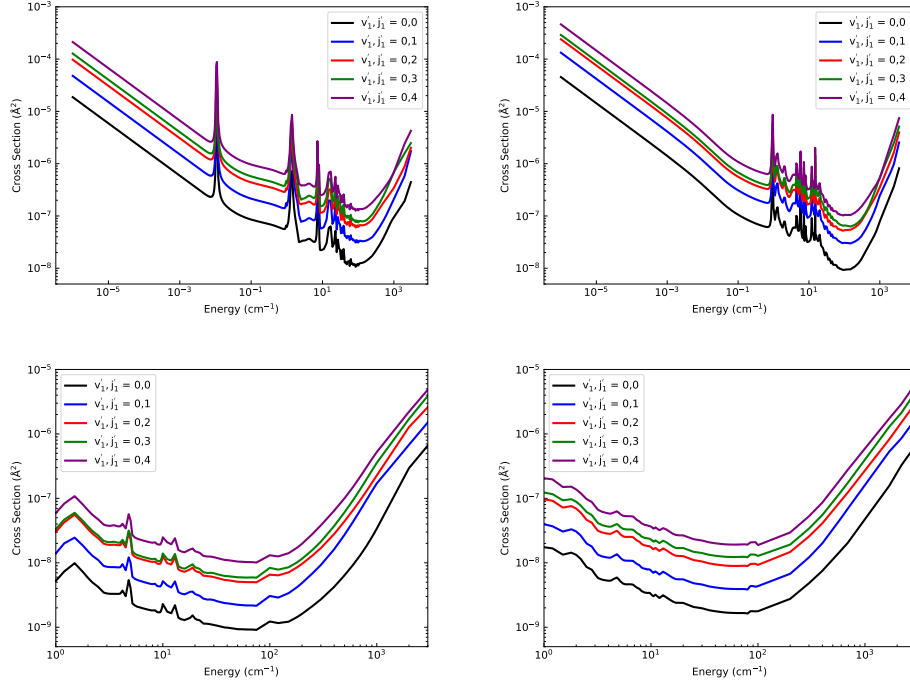


Figure 8. 6D-CC cross sections for vibrational relaxation of HCl induced by collisions with H₂. The upper panels show results for relaxation from HCl($v_1 = 1, j_1 = 0$) to HCl($v'_1 = 0, j'_1 = 0 - 4$), while the lower panels show them for transitions from HCl($v_1 = 1, j_1 = 5$) to HCl($v'_1 = 0, j'_1 = 0 - 4$). The left panels show results with para-H₂($v_2 = 0, j_2 = 0$) as the perturber, while the right panels show them for ortho-H₂($v_2 = 0, j_2 = 1$).

5.2. *Vibrationally inelastic transitions*

Selected 5D-CS rates for vibrationally inelastic collisions are shown in Fig. 14. The rates increase smoothly with temperature and exhibit a propensity for $\Delta j_1 = \Delta F_1$ transitions. The propensity rule tends to be obeyed more strongly for $F_1 = j_1 + 3/2$ than for the lower values of F_1 (e.g., compare upper and lower panels of Fig. 14). The dominant $\Delta j_1 = \Delta F_1$ transition is shown in Fig. 15 for a sample of initial $F_1 = j_1 + 3/2$ states. The curves are smoothly varying and monotonic as the value of j_1 is increased. The rates for transitions induced by para-H₂ tend to be a bit higher than for those induced by ortho-H₂. The curves increase with Δj_1 due to the decreasing internal energy gaps between the initial and final states. The pattern eventually stops around $\Delta j_1 = 12$ due to the large internal angular momentum change. The rate coefficients then substantially decrease as the calculations approach the edge of the basis set, indicating that convergence has been achieved. While fully converged with respect to the basis set, we nevertheless expect, based on the spin-free results, that these rate coefficients are less accurate than the vibrationally elastic results shown in Fig. 13. The qualitative trends, however, are expected to be reliable.

6. ASTROPHYSICAL APPLICATIONS

To date rovibrational transitions of HCl in the interstellar medium have only been detected in observations in the bright infrared source CRL 2136 by Goto et al. (2013). Using the CRILES spectrograph on the VLT on Paranal and the IRCS spectrograph on the Subaru Telescope on Mauna Kea, the $v = 0 \rightarrow 1$ $P(0) - P(7)$, $R(0) - R(3)$, and $R(5)$ lines were observed in absorption likely from the circumstellar envelope or disk. From the equivalent absorption widths, the column densities were deduced for rotational states in $v = 0$ (Goto et al. 2013) as reproduced in Figure 16. Using a collisional-radiative model, the best fit to the observations for an assumed density of $n(\text{H}_2) > 10^9 \text{ cm}^{-3}$ was a kinetic temperature of 250 K and a reduced column density $N(\text{HCl})/v = 3 \times 10^{14} \text{ cm}^{-2}/(\text{kms}^{-1})$, where v is the collision velocity broadening (Goto et al. 2013). The straight line fit through the observed data, as shown in the rotational population diagram of Figure 16, indicates that the population of the $v = 0$ rotational levels are in LTE. Further, details of the model in Goto et al. (2013) are unknown.

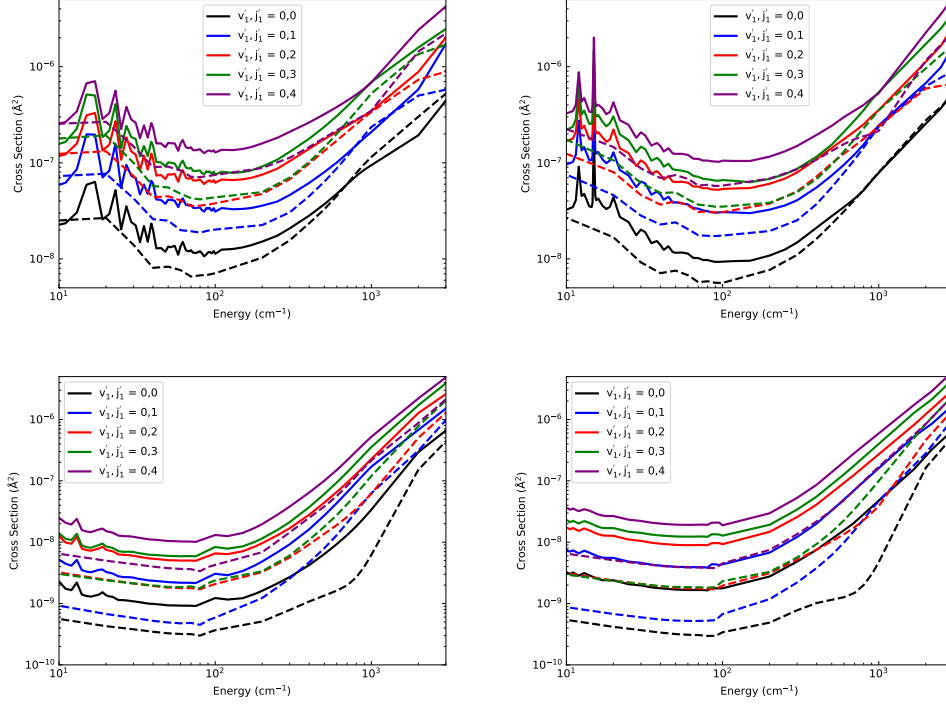


Figure 9. Comparison between 6D-CC (solid lines) and 5D-CS (dashed lines) cross sections for rovibrational relaxation from $\text{HCl}(v_1 = 1, j_1 = 0)$ (top panels) and $\text{HCl}(v_1 = 1, j_1 = 5)$ (bottom panels) to $\text{HCl}(v'_1 = 0, j'_1 = 0 - 4)$ induced by collisions with para- $\text{H}_2(v_2 = 0, j_2 = 0)$ (left panels) and ortho- $\text{H}_2(v_2 = 0, j_2 = 1)$ (right panels).

Using the new $\text{HCl}-\text{H}_2$ collisional data presented here, we performed a NLTE collisional-radiative model of HCl using the radiative transfer package RADEX (van der Tak et al. 2007). The model considered a constant density and temperature uniform sphere with conditions nearly the same as in Goto et al. (2013), except we use a density of $n(\text{H}_2) = 10^{10} \text{ cm}^{-3}$. The fit to the kinetic temperature of 250 K is reproduced as well as the column density. Varying only the kinetic temperature, a range of NLTE rotational population results are also given in Figure 16. Future models will consider radiative pumping due to the bright IR source.

Considering higher temperature, but lower density regimes, grids of NLTE models were performed to compute $v = 1 \rightarrow 0$ rovibrational line emission ratios as given in Figure 17. Four different line ratios are considered which may have temperature and density diagnostic potential for future observations of HCl emission near $3.5 \mu\text{m}$. For densities larger than $\sim 10^7 \text{ cm}^{-3}$ the considered line ratios are insensitive to density, but may be useful temperature probes. Conversely, for lower densities, the $P(1)/P(2)$, $P(1)/R(1)$, and $R(2)/R(3)$ line ratios are sensitive to the density, but less so to temperature.

7. DISCUSSION

Cross sections and rate coefficients for transitions induced by H_2 within the first vibrational band of HCl are needed for astrophysical models of molecular clouds. This work has reported the first set of rovibrational cross sections using a fully 6D-PES. Selected results were computed within the numerically exact 6D-CC formulation. These 6D-CC calculations were performed over a wide range of collision energies for transitions from $\text{HCl}(v_1 = 0, j_1 = 0)$ to $\text{HCl}(v'_1 = 0, j'_1 = 0 - 16)$ induced by para- H_2 , and for transitions from $\text{HCl}(v_1 = 1, j_1 = 0 \text{ or } 5)$ to $\text{HCl}(v'_1 = 0 \text{ or } 1, j'_1)$ induced by ortho- and para- H_2 .

A reduced-dimensionality coupled-states approximation (5D-CS) formulation was used to determine results for $\text{HCl}(v_1 = 0, j_1 = 0 - 20)$ and $\text{HCl}(v_1 = 1, j_1 = 0 - 10)$. The cross sections and rate coefficients were benchmarked against the 6D-CC results, along with available rate coefficients in the BASECOL database (Dubernet et al. 2013), and they were shown to be within less than 30% for vibrationally elastic transitions, and within a factor of 2-10 for vibrationally inelastic transitions. The relatively large error in some of the rovibrational transitions is due to neglect-

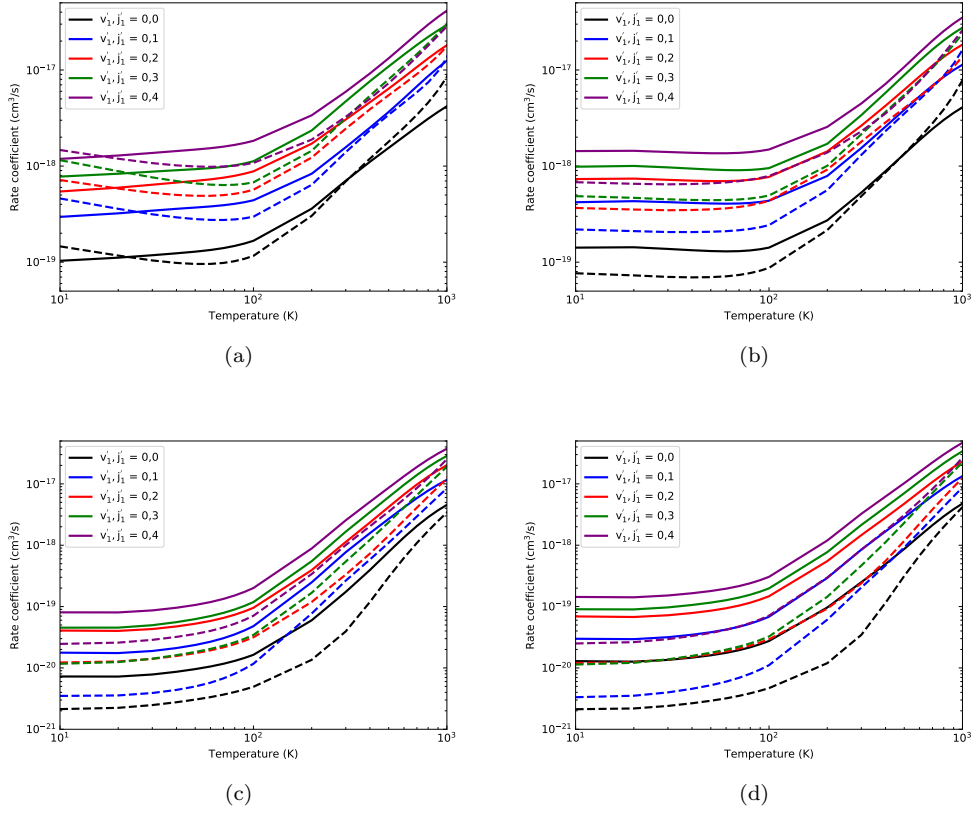


Figure 10. A similar comparison as in Fig. 9, but for rate coefficients as a function of temperature. The 6D-CC rates are shown as solid lines, while the 5D-CS results are shown as dashed lines.

ing both the Coriolis kinetic coupling and the twist angle dependence of the PES. Unlike $\text{SO}+\text{H}_2$, where most of the sensitivity to twist angle occurred near the repulsive wall of the potential (Price et al. 2021), the present system is more sensitive to the twist angle in the vicinity of the potential minimum. This suggests that the 5D-CS formulation may be less accurate for vibrationally inelastic transitions in the present system. Nevertheless, the computational efficiency of the formulation and the prospects for correcting the errors with selected 6D-CC results via machine learning (Jasinski et al. 2020) make it a good starting point for constructing a complete database of state-resolved rate coefficients.

Hyperfine-resolved 5D-CS results for pure rotational transitions were benchmarked against available rate coefficients in the BASECOL database (Dubernet et al. 2013) and shown to be in good agreement. The present results for hyperfine-resolved rovibrational transitions are the first of their kind and can serve as an adequate placeholder until more reliable data becomes available.

The current rovibrational $\text{HCl}-\text{H}_2$ rate coefficients were adopted to a non-LTE model of the IR bright source CRL 2136 and found to reproduce the kinetic temperature and column density deduced by observations. Some example rovibrational line ratios were found to be potential temperature or density diagnostics for NLTE environments. The present cross sections and rate coefficients can be obtained on the UGA Molecular Excitation database (sites.physast.uga.edu/amdbs) with the latter available in both LAMDA (van der Tak et al. 2020) and BASECOL (Dubernet et al. 2013) format to aid the astrophysical modeling community.

This work was supported by NASA grant NNX16AF09G and NSF grants PHY-1806180 & PHY-2110227. We thank Hua Guo for many helpful discussions.

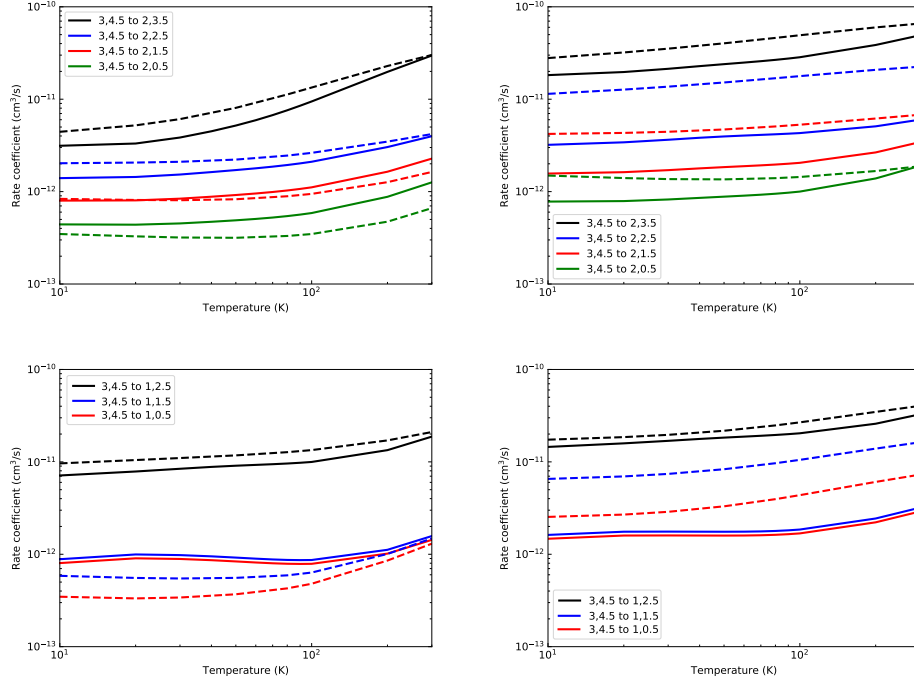


Figure 11. Comparison between 5D-CS (solid lines) and 4D-CC rigid rotator (Lanza et al. 2014b) (dashed lines) rate coefficients for transitions from $\text{HCl}(v_1 = 0, j_1 = 3, F_1 = 4.5)$ induced by para- $\text{H}_2(v_2 = 0, j_2 = 0)$ (left) and ortho- $\text{H}_2(v_2 = 0, j_2 = 1)$ (right). In the upper panels, the final rotational level of HCl is $j'_1 = 2$, while in the lower panels $j'_1 = 1$.

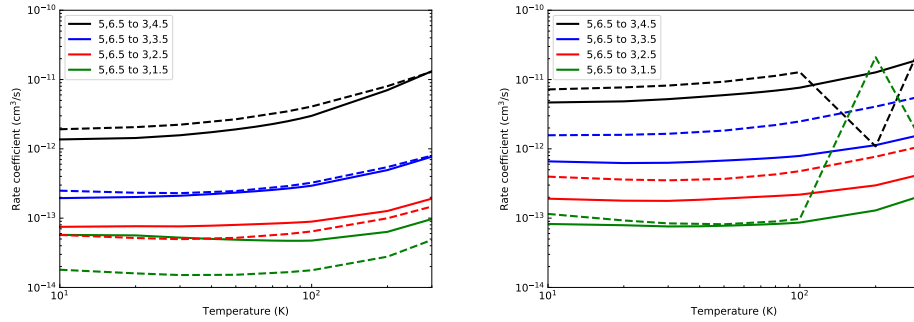


Figure 12. Comparison between 5D-CS (solid lines) and 4D-CC rigid rotator (Lanza et al. 2014b) (dashed lines) rate coefficients for transitions from $\text{HCl}(v_1 = 0, j_1 = 5, F_1 = 6.5)$ induced by para- $\text{H}_2(v_2 = 0, j_2 = 0)$ (left) and ortho- $\text{H}_2(v_2 = 0, j_2 = 1)$ (right). The final rotational level of HCl is $j'_1 = 3$.

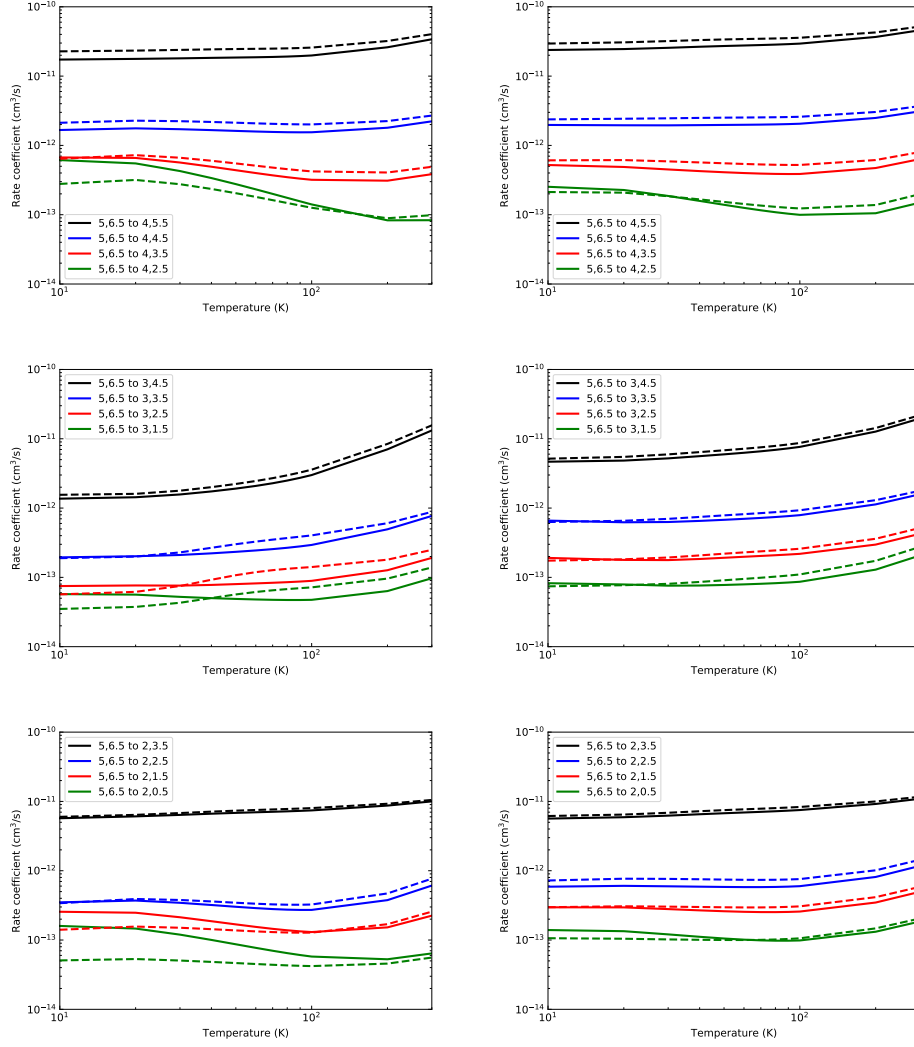


Figure 13. Comparison between 5D-CS hyperfine-resolved rate coefficients for transitions within $v_1 = 0$ (solid lines) and within $v_1 = 1$ (dashed lines). The rate coefficients are for transitions from $\text{HCl}(v_1 = 0, j_1 = 5, F_1 = 6.5)$ induced by para- $\text{H}_2(v_2 = 0, j_2 = 0)$ (left) and ortho- $\text{H}_2(v_2 = 0, j_2 = 1)$ (right). In the upper panels, the final rotational level of HCl is $j'_1 = 4$, in the middle panels $j'_1 = 3$, and in the lower panels $j'_1 = 2$

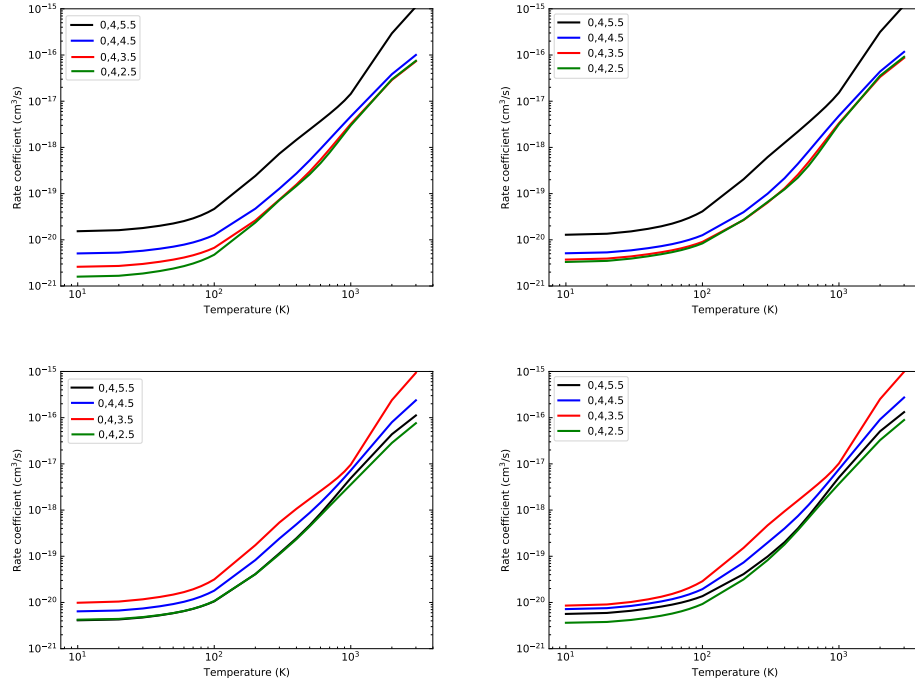


Figure 14. 5D-CS hyperfine-resolved results for para-H₂ (left) and ortho-H₂ (right) for $v_1 = 1$ to 0. The top panels show results for transitions from $(v_1, j_1, F_1) = (1, 5, 6.5)$ to $(0, 4, F'_1)$, while the bottom panels show transitions from $(v_1, j_1, F_1) = (1, 5, 4.5)$ to $(0, 4, F'_1)$

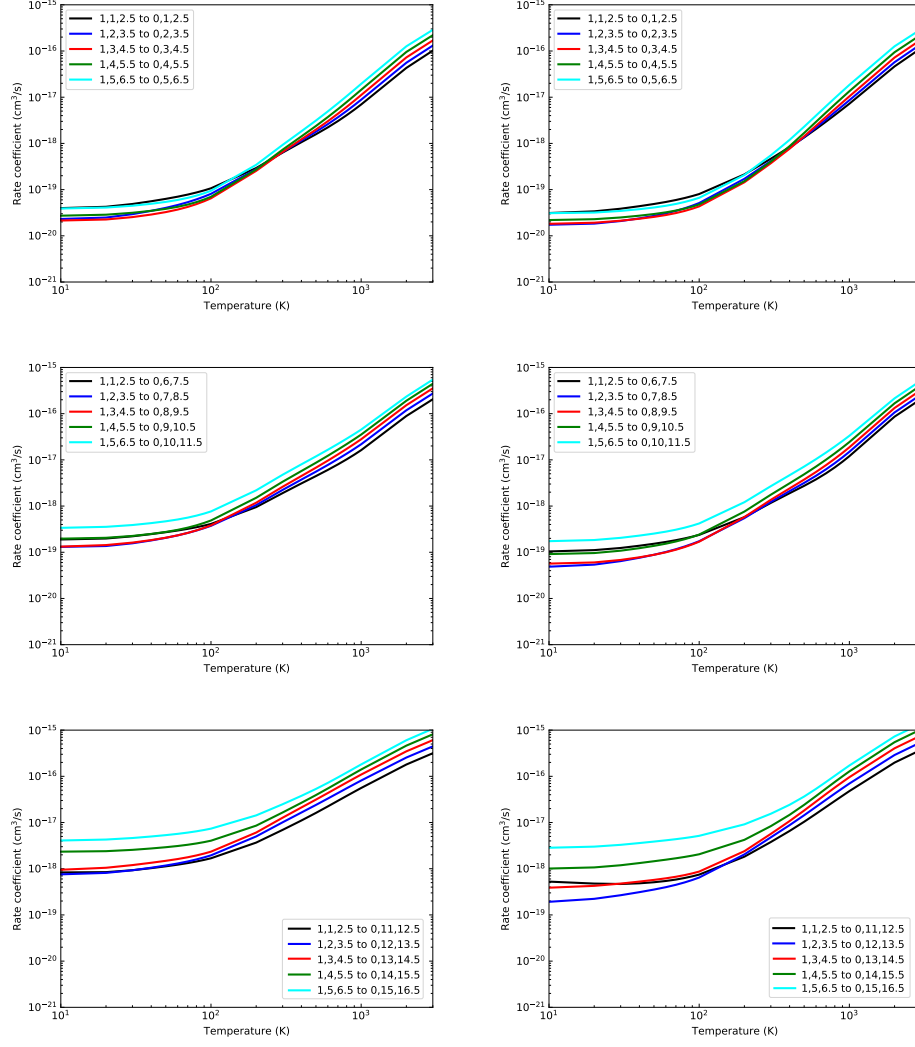


Figure 15. 5D-CS hyperfine-resolved results for vibrational relaxation from $v_1 = 1$ to $v_1 = 0$ induced by para- H_2 (left) and ortho- H_2 (right). These results are for transitions in which $\Delta j_1 = \Delta F_1$, with $F_1 = j_1 + 1.5$ and $\Delta j_1 = 0$ (top panels), 5 (middle panels), and 10 (bottom panels).

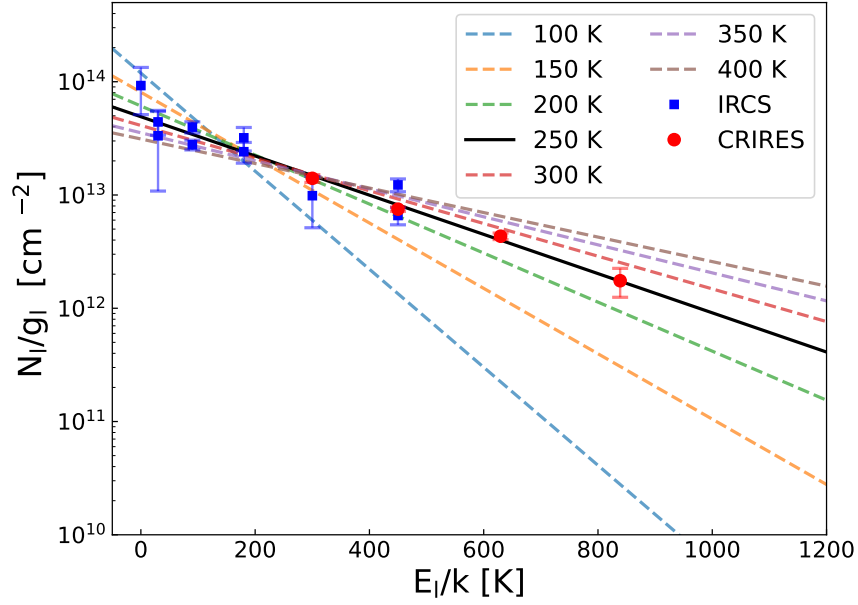


Figure 16. HCl rotational population diagram for $v = 0$ from NLTE calculations using the current HCl-H₂ collisional rate coefficients. Lines correspond to the indicated kinetic temperature while the symbols are the measured column density divided by the lower-level statistical weight from observations of CRL 2136 (Goto et al. 2013). Models were performed with $n(\text{H}_2) = 10^{10} \text{ cm}^{-3}$, $N(\text{HCl})/v = 3 \times 10^{14} \text{ cm}^{-2}/(\text{km/s}^{-1})$, and the cosmic microwave background.

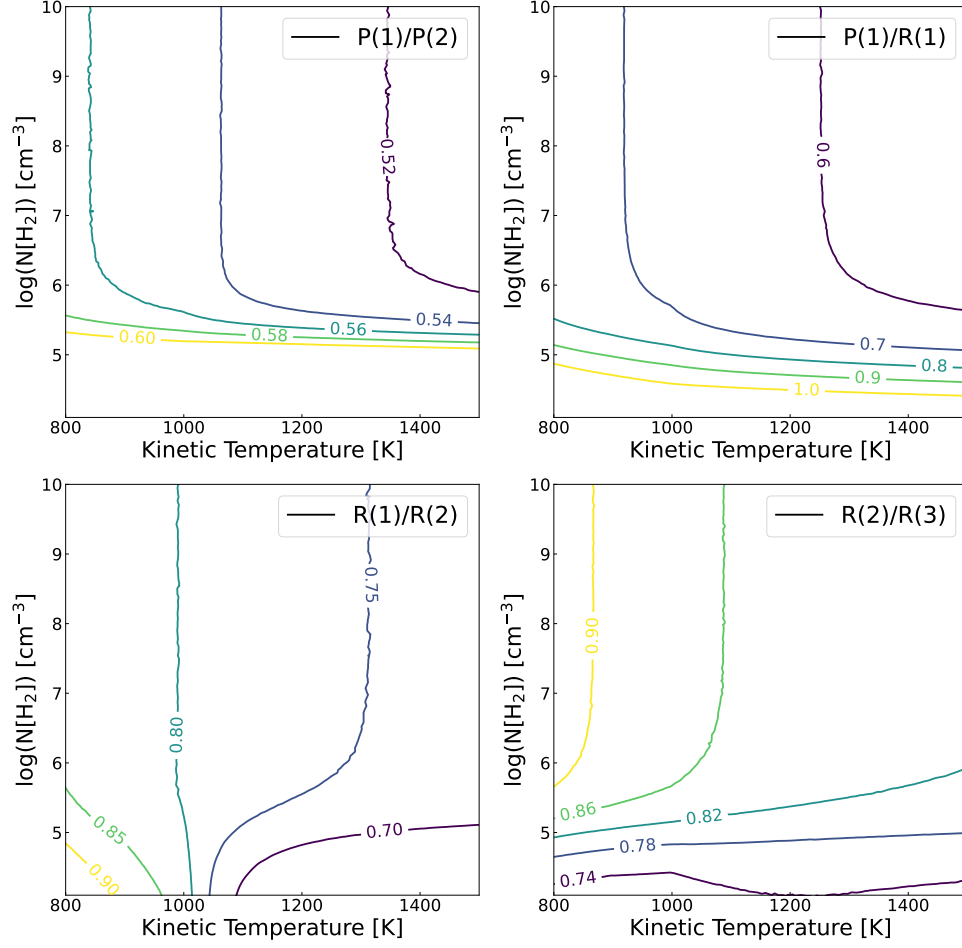


Figure 17. HCl rovibrational diagnostic emission line ratios for $v = 1 \rightarrow 0$ for the indicated transitions as a function of kinetic temperature and density. The ratios were obtained from NLTE models assuming $N(\text{HCl})/v = 3 \times 10^{14} \text{ cm}^{-2}/(\text{kms}^{-1})$ and radiation due to the cosmic microwave background.

REFERENCES

- Alexander, M. H., & DePristo, A. E. 1977, *J. Chem. Phys.*, 66, 2166
- Alkorta, I., Elguero, J., & Bene, J. E. D. 2010, *Chem. Phys. Lett.*, 489, 159
- Anderson, D. T., Schuder, M., & Nesbitt, D. J. 1998, *Chem. Phys.*, 239, 253
- Blake, G. A., Keene, J., & Phillips, T. G. 1985, *Astrophys. J.*, 295, 501
- Burton, H., Mysliwiec, R., Forrey, R. C., et al. 2018, *Mol. Astrophys.*, 11, 23
- Cernicharo, J., Goicoechea, J. R., Daniel, F., et al. 2010, *A&A*, 518, L115.
<https://doi.org/10.1051/0004-6361/201014638>
- Codella, C., Ceccarelli, C., Bottinelli, S., et al. 2011, *The Astrophysical Journal*, 744, 164.
<https://doi.org/10.1088/0004-637x/744/2/164>
- Corey, G., & McCourt, F. 1983, *J. Phys. Chem.*, 87, 2723
- Dubernet, M.-L., Alexander, M. H., Ba, Y. A., et al. 2013, *Astron. Astrophys.*, 553, 50
- Forrey, R. C., Yang, B., Stancil, P., & Balakrishnan, N. 2015, *Chem. Phys.*, 462, 71
- Goto, M., Usuda, T., Geballe, T. R., et al. 2013, *Astron. Astrophys.*, 558, L5
- Green, S. 1975, *J. Chem. Phys.*, 62, 2271
- Heil, T. G., Green, S., & Kouri, D. J. 1978, *J. Chem. Phys.*, 68, 2562
- Jasinski, A., Montaner, J., Forrey, R. C., et al. 2020, *Phys. Rev. Research*, 2, 032051(R)
- Kama, M. 2015, *Astron. Astrophys.*, 574, A107
- Korablev, O. 2021, *Science Advances*, 7
- Krasnopolsky, V. A. 2010, *Icarus*, 208, 539. <https://www.sciencedirect.com/science/article/pii/S0019103510000862>
- Lanza, M., Kalugina, Y., Wiesenfeld, L., Faure, A., & Lique, F. 2014a, *MNRAS*, 443, 3351
- Lanza, M., Kalugina, Y., Wiesenfeld, L., & Lique, F. 2014b, *J. Chem. Phys.*, 140, 064316
- Lanza, M., & Lique, F. 2014, *J. Chem. Phys.*, 141, 164321
- Monje, R. R., Lis, D. C., Roueff, E., et al. 2013, *The Astrophysical Journal*, 767, 81.
<https://doi.org/10.1088/0004-637x/767/1/81>
- Morita, M., Yao, Q., Xie, C., Guo, H., & Balakrishnan, N. 2020, *Phys. Rev. Research*, 2, 032018(R)
- Morita, M., Zuo, J., Guo, H., & Balakrishnan, N. 2021, *J. Chem. Phys.*, 154, 104304
- Offer, A. R., van Hemert, M. C., & van Dishoeck, E. F. 1994, *J. Chem. Phys.*, 100, 362
- Olsen, K. S. 2021, *Astron. Astrophys.*, 647, A161
- Peng, R., Yoshida, H., Chamberlin, R. A., et al. 2010, *Astrophys. J.*, 723, 218
- Price, T. J., Forrey, R. C., Yang, B. H., & Stancil, P. C. 2021, *J. Chem. Phys.*, 154, 034301
- Schilke, P., Phillips, T. G., & Wang, N. 1995, *Astrophys. J.*, 441, 334
- Teanby, N., Gould, B., & Irwin, P. 2021, *Icarus*, 354, 114045. <https://www.sciencedirect.com/science/article/pii/S0019103520303997>
- van der Tak, F. F. S., Black, J. H., Schöier, F. L., Jansen, D. J., & van Dishoeck, E. F. 2007, *A&A*, 468, 627
- van der Tak, F. F. S., Lique, F., Faure, A., Black, J. H., & van Dishoeck, E. F. 2020, *Atoms*, 8, 15
- Yang, B., Zhang, P., Qu, C., et al. 2020, *Chem. Phys.*, 532, 110695
- . 2018, *J. Phys. Chem. A*, 122, 1511
- Yao, Q., Morita, M., Xie, C., Balakrishnan, N., & Guo, H. 2019, *J. Phys. Chem. A*, 123, 6578